AGU PUBLICATIONS

JGR

Journal of Geophysical Research: Solid Earth

RESEARCH ARTICLE

10.1002/2016JB013078

Key Points:
- Comprehensive directivity study on fluid-induced microseismic events applying an EGF technique
- Rupture directivity is predominantly unilateral and shows dependencies on distance and magnitude
- Largest microseismic events nucleate at the reservoir rim and rupture back toward the borehole

Correspondence to:
J. Folesky,
jonas.folesky@geophysik.fu-berlin.de

Citation:
Folesky, J., J. Kummerow, S. A. Shapiro, M. Häring, and H. Asanuma (2016), Rupture directivity of fluid-induced microseismic events: Observations from an enhanced geothermal system, *J. Geophys. Res. Solid Earth*, *121*, 8034–8047, doi:10.1002/2016JB013078.

Received 8 APR 2016
Accepted 8 OCT 2016
Accepted article online 12 OCT 2016
Published online 9 NOV 2016
Corrected 23 APR 2019

This article was corrected on 23 APR 2019. See the end of the full text for details.

©2016. American Geophysical Union. All Rights Reserved.

Rupture directivity of fluid-induced microseismic events: Observations from an enhanced geothermal system

Jonas Folesky[1], Jörn Kummerow[1], Serge A. Shapiro[1], Markus Häring[2], and Hiroshi Asanuma[3]

[1]Department of Geophysics, Freie Universität Berlin, Berlin, Germany, [2]Geo Explorers Ltd., Liestal, Switzerland, [3]North Japan Research Institute for Sustainable Energy, Hirosaki University, Aomori, Japan

Abstract The rupture process of fluid-induced microseismic events is still poorly understood, mainly due to usually small magnitudes and sparse monitoring geometries. The high-quality recordings of the earthquake sequence 2006–2007 at the enhanced geothermal system at Basel, Switzerland, constitute a rare exception, allowing a systematic directivity study of 195 events using the empirical Green's function method. We observe clear directivity signatures for about half the events which demonstrates that rupture directivity persists down to small magnitudes ($M_L \sim 1$). The predominant rupture behavior is unilateral. We further find evidence that directivity is magnitude dependent and varies systematically with distance from the injection source. Whereas pore pressure seems to play the dominant role close to the injection source and no preferred rupture direction is observable, directivity aligns parallel to the event distribution with increasing distance ($\gtrsim$100 m) and is preferably oriented away from the injection point. The largest analyzed events ($M_L \sim 2$) show a distinct behavior: They rupture toward the injection source, suggesting that they nucleate in the vicinity of the pressure front and propagate backward into the perturbed volume. This finding is of particular relevance for seismic hazard assessment of georeservoirs, since it implies that maximum event size is related to dimension of the fluid-perturbed volume. Our study also resolves rupture complexities for a small group of events. This shows that small fault heterogeneities exist down to a scale of a few tens of meters. The observation of directivity and complexity in induced microseismic events suggest that future source studies account for these phenomena.

1. Introduction

For numerous large- and moderate-sized earthquakes rupture directivity has been retrieved successfully from azimuthal variations of seismic pulse length, amplitude, and source spectra [e.g., *Ben-Menahem*, 1961; *Boatwright and Boore*, 1982; *Frankel and Kanamori*, 1983]. *Boatwright* [2007], *Dreger et al.* [2007], *Kane et al.* [2013], and *Taira et al.* [2015] found evidence for rupture directivity of small ($2 \leq M \leq 5$) natural earthquakes. Observations of directivity effects from fluid-induced microseismic events ($M \leq 2$), however, are to date only sparse and restricted to few events [*Li et al.*, 1995; *Jost et al.*, 1998], and particularly, their rupture processes have remained poorly understood. In contrast to large earthquakes, where unilateral ruptures seem to prevail [*McGuire et al.*, 2002], simple circular fault models [*Brune*, 1970; *Madariaga*, 1976; *Boatwright*, 1980] are generally invoked in the microseismic context when source parameter studies are performed [e.g., *Goertz-Allmann et al.*, 2011]. These studies implicitly assume ideal circular and hence symmetric ruptures which exhibit no rupture directivity, although a reliable empirical knowledge on spatiotemporal rupture characteristics is missing due to the poor resolution and sparse geometries of microseismic monitoring systems.

But what should be considered if clear signatures of directivity are indeed identified also in fluid-induced microseismic data? This will then require more complex rupture models that comprise directivity [e.g., *Madariaga*, 1976; *Kaneko and Shearer*, 2015], or it could suggest the application of models like unilateral or bilateral ruptures [e.g., *Haskell*, 1964]. A distinction between the different models within a source study would allow to improve the characterization of microseismic source parameters (e.g., fault size and stress drop) and could also be valuable for an enhanced hazard assessment of fluid-induced microseismicity. In fact, several studies of natural [*Dreger et al.*, 2007; *Taira et al.*, 2015] and mining-induced seismicity [*Yamada et al.*, 2005; *Kwiatek et al.*, 2011] found indications for rupture complexity of microearthquakes. *Dreger et al.* [2007] and *Taira et al.* [2015] identified complex slip behavior, high stress drop, and directivity for small natural events in California. *Yamada et al.* [2005] analyzed the source parameters of small events at the Mponeng gold mine,

South Africa, and observed values typical for larger natural seismicity. For the same gold mine *Kwiatek et al.* [2011] deduced self-similar behavior of seismic events even down to magnitudes as small as $M_W \sim -4$.

The objective of this study is to perform for the first time a comprehensive, empirical study of rupture directivity for fluid-induced microseismicity. Additionally, we describe examples of complex rupture behavior for microseismic sources. We use high-quality waveforms of microseismicity recorded at the Basel-Enhanced Geothermal System, Switzerland, during and after the stimulation in 2006–2007 [*Häring et al.*, 2008]. The event magnitude range is $0.0 \leq M_L \leq 3.4$. Using multiplet analysis, we select pairs of colocated events with similar source mechanisms and perform an empirical Green's functions (EGF) analysis [*Mueller*, 1985; *Li et al.*, 1995] in order to reconstruct the relative source time functions (RSTFs) of the seismic events for each station. Rupture directivity is then inferable from systematic variations of amplitude or duration of the RSTFs with station azimuth [*Savage*, 1965]. We subsequently examine the spatial and temporal distribution of the obtained rupture orientations and directivity and analyze possible controlling factors. Specifically, we find a dependence of rupture directivity on event size and distance from the injection source.

2. Data: The Induced Microseismicity at the Basel EGS

In this study we use about 2800 microseismic events which were induced during the stimulation of the Basel-1 geothermal site, Switzerland, in December 2006 and also during several months of the postinjection phase until June 2007 [*Häring et al.*, 2008]. The microseismicity was monitored by a network of six azimuthally well distributed three-component downhole receivers within a distance of up to 5 km from the injection source (Figure 1). Sampling rate for all receivers was 1 kHz. The located microseismic event cloud centers at a depth of about 4.5 km and extends about 1 km in horizontal and also about 1 km in vertical direction. The seismicity shows a subvertical, north-north-west to south-south-east orientation which almost coincides with the direction of the maximum horizontal stress, S_{Hmax} [*Häring et al.*, 2008; *Dyer et al.*, 2010]. We use refined event locations, based on multiplet analysis and optimized *P* and *S* phase arrival times [*Kummerow et al.*, 2011; *Reshetnikov et al.*, 2015]. The event magnitudes range between $0.0 \leq M_L \leq 3.4$, and the largest events occurred during and after the late phase of the injection experiment. The predominant source mechanisms of the Basel events are strike-slip and oblique faulting [*Deichmann and Giardini*, 2009; *Kraft and Deichmann*, 2014].

Deichmann and Giardini [2009] found that nearly all large events were situated at the outer rim of the actual extent of the microseismic cloud. Studies by *Catalli et al.* [2013] and *Goertz-Allmann et al.* [2011] indicate that seismicity attributes at Basel correlate with the pore pressure, which itself decreases with the distance from the injection source [*Dinske and Shapiro*, 2010]. *Goertz-Allmann et al.* [2011] found an increase of average stress drop with increasing radial distance and decreasing pore pressure, and *Catalli et al.* [2013] observed that the performance of their Coulomb model improves progressively with increasing distance (i.e., decreasing influence of the pore pressure). *Kummerow et al.* [2014] also noted that the distribution of repeating earthquakes at Basel is particularly sensitive to the pore pressure.

3. Method: Empirical Green's Functions and Directivity Effect

A recorded seismogram can be described as the convolution of four time series, e.g.,

$$u(t) = s(t) * p(t) * r(t) * i(t), \tag{1}$$

where $u(t)$ is the recorded seismogram, $s(t)$ is the source time function, $p(t)$ is the impulse response of the path, $r(t)$ is the influence of the recording site, and $i(t)$ is the instrument response. The aim of the empirical Green's function (EGF) method is to compute a relative source time function (RSTF) for a larger event, assuming that it is colocated with a smaller event with a similar focal mechanism [e.g., *Mueller*, 1985; *Frankel et al.*, 1986; *Mori*, 1993]. Then, the source time function of the smaller event is approximately a delta pulse, $s(t) \approx \delta(t)$, and the seismogram of the smaller event is deconvolved from the seismogram of the larger event to obtain the relative source time function. In the frequency domain, this can be expressed as

$$\frac{|U(\omega)|}{|\mathrm{EGF}(\omega)|} \approx \frac{|S(\omega) \cdot P(\omega) \cdot R(\omega) \cdot I(\omega)|}{|\delta(\omega) \cdot P(\omega) \cdot R(\omega) \cdot I(\omega)|} = \frac{|S(\omega)|}{|\delta(\omega)|} = |S'(\omega)|, \tag{2}$$

where $\mathrm{EGF}(\omega)$ is the spectrum of the smaller event and $S'(\omega)$ is the RSTF (relative to the seismic moment of the smaller event), since the effects of path, receiver site, and instrument response are equal and can be

21699356, 2016, 11, Downloaded from https://agupubs.onlinelibrary.wiley.com/doi/10.1002/2016JB013078 by Cochrane Germany, Wiley Online Library on [23/01/2024]. See the Terms and Conditions (https://onlinelibrary.wiley.com/terms-and-conditions) on Wiley Online Library for rules of use; OA articles are governed by the applicable Creative Commons License

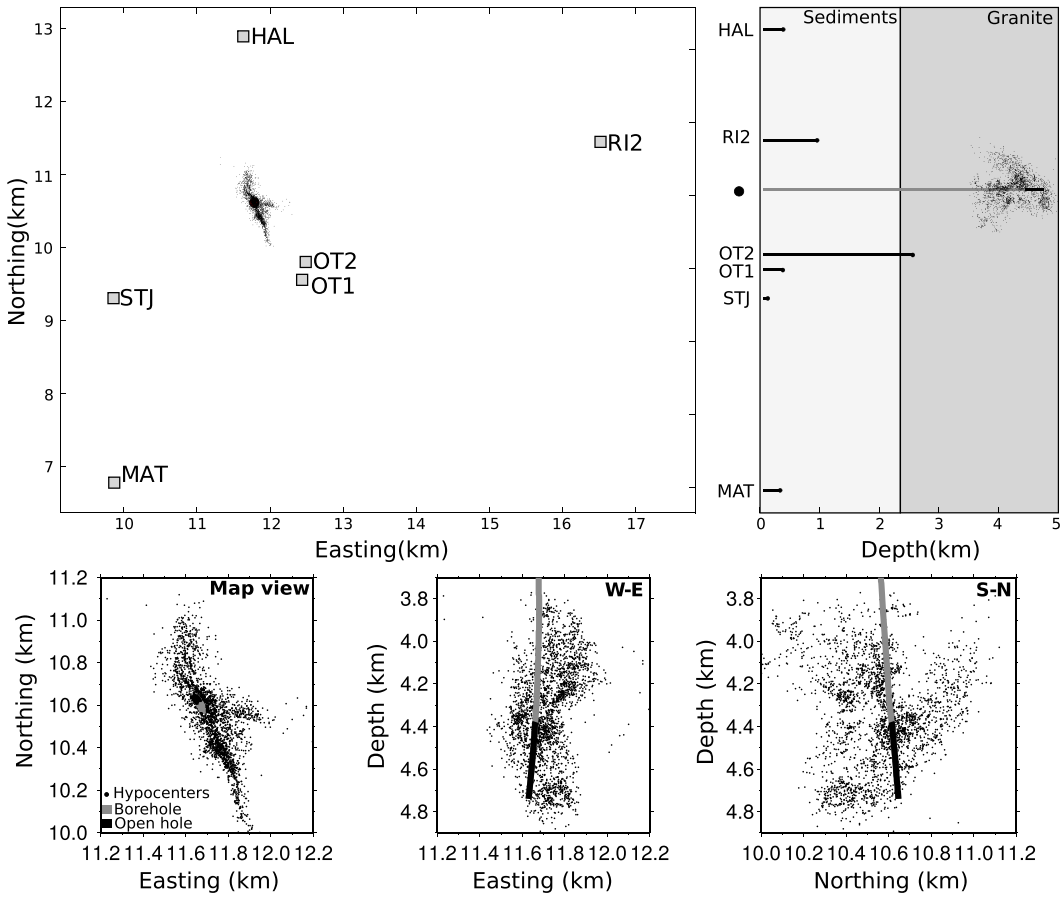

Figure 1. (top row) Station distribution and microseismic event cloud at the Basel EGS. The station geometry is displayed in map view and in a schematic depth view. (bottom row) The microseismicity is shown in map and depth views together with the borehole and open hole section.

eliminated. The technique of spectral division is described by, e.g., *Mueller* [1985], *Li et al.* [1995], and *Vallée* [2004]. This deconvolution is only valid for frequencies below the corner frequency of the EGF spectrum, where the delta pulse assumption of the EGF holds (this means that $\delta(\omega)$ is a constant). In practice the procedure sometimes needs stabilization, e.g., by a water level correction [*Mueller*, 1985] or a Gaussian filter for both numerator and denominator [*Li et al.*, 1995] or the application of the Projected Landweber Method [*Vallée*, 2004].

For propagating ruptures the RSTF exhibits variations of amplitudes and duration as a function of the rupture-receiver geometry. *Savage* [1965] derived the following formula

$$F = \frac{A}{K} = \frac{i \cdot v_r}{1 - (v_r/c)^i \cdot \cos^i(\phi - \phi_0) \cdot \sin^i(\theta - \theta_0)}, \tag{3}$$

where F describes the expected amplitude A at a given station, scaled by an unknown constant K. v_r is the rupture velocity and c is the phase velocity, respectively. ϕ is the station azimuth relative to the hypocenter and θ is the station plunge. As the rupture plane is assumed to be vertical, the angles ϕ_0 and θ_0 are sufficient to describe the rupture geometry. ϕ_0 is the azimuthal orientation of the rupture plane and θ_0 describes the tilt of the rupture direction inside that rupture plane. The coordinate system is illustrated in Figure 2. The formula describes unilateral ruptures for $i = 1$ and bilateral ruptures for $i = 2$. A similar expression is given for the modulation of the source duration

$$T = \frac{L}{i \cdot v_r} \cdot \left(1 - (v_r/c)^i \cdot \cos^i(\phi - \phi_0) \cdot \sin^i(\theta - \theta_0)\right), \tag{4}$$

21699356, 2016, 11, Downloaded from https://agupubs.onlinelibrary.wiley.com/doi/10.1002/2016JB013078 by Cochrane Germany, Wiley Online Library on [23/01/2024]. See the Terms and Conditions (https://onlinelibrary.wiley.com/terms-and-conditions) on Wiley Online Library for rules of use; OA articles are governed by the applicable Creative Commons License

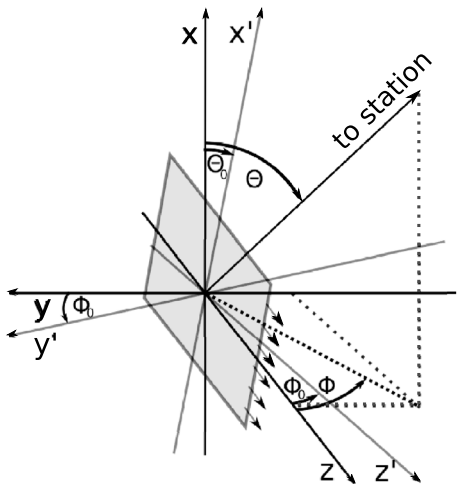

Figure 2. Coordinate system after *Savage* [1965] which was used to describe a propagating rupture for strike-slip and dip-slip dislocations. The vertical axis (X) is the depth axis. The small arrows depict the rupture direction on the fault plane (gray). The primed axes describe the orientation of the rupture plane. ϕ_0 is the rotation around the X axis, and θ_0 is the rotation around the plane normal, the Y' axis. Note that although ϕ is defined counterclockwise in the original publication, as it is drawn here, equation (3) also allows to use the azimuth instead.

where all arguments are the same as in equation (3) and T and L are the apparent rupture duration and the rupture length, respectively. The difference in observed rupture duration, e.g., for unilateral rupture can be substantial. Assuming a rupture velocity of $v_r = 0.8 \cdot c$ and defining a rupture duration $T_0 = L/v_r$, one obtains possible apparent rupture durations between $T = T_0 \cdot (1 \pm 0.8)$ for stations in backward and forward direction of the rupture, respectively.

4. Processing

We first identify pairs of events which are suitable for the EGF analysis by calculating their waveform similarity and interevent distance. We restrict our similarity analysis to the deepest borehole sensor (OT2) which is closest to the induced seismicity cloud and most sensitive to minor variations of seismic waveforms. Waveform similarity is determined for all possible combinations of event pairs by calculating maximum normalized cross-correlation coefficients, cc, for a seismogram window of 0.6 s length which includes both the P and the S phase at OT2, in the frequency band 1–60 Hz. We use the arithmetic mean of the cross-correlation coefficients on all three sensor components and only consider event pairs with $cc > 0.8$. For the application of the EGF method we additionally require a minimum magnitude difference between events of each event pair of $\Delta M = 0.6$ allowing on the one hand the identification of a sufficient number of event pairs and on the other hand to uphold the delta pulse assumption. This results in a selection of 195 suitable event pairs whose larger event partners show a magnitude range of $0.90 \leq M_L \leq 2.35$.

In a second step we apply an EGF analysis procedure which is similar to the one described in *Li et al.* [1995]. We first cut 2 s time windows of the S phase from the three-component displacement seismograms. In the next step zeroes are added before and after the signal and a Fourier transform is performed. In the spectral division the smaller EGF events are used in the denominator, and thus, we high cut all spectra at 100 Hz to reduce the effect of high-frequency noise. The spectra are slightly smoothed by a Gaussian filter to further ensure the stability of the spectral division [*Mueller*, 1985; *Li et al.*, 1995]. Next, the amplitude spectra of the two partner events are divided, and their phase spectra are subtracted. The resulting spectrum is then back transformed into time domain. Ideally, the procedure is stable on all three components at each record; however, to ensure good quality, we compare the three componentwise reconstructed RSTFs and in case of a good match they are averaged to enhance stability further [cf. *Dreger et al.*, 2007; *Harrington and Brodsky*, 2009]. If one of the

21699356, 2016, 11, Downloaded from https://agupubs.onlinelibrary.wiley.com/doi/10.1002/2016JB013078 by Cochrane Germany, Wiley Online Library on [23/01/2024]. See the Terms and Conditions (https://onlinelibrary.wiley.com/terms-and-conditions) on Wiley Online Library for rules of use; OA articles are governed by the applicable Creative Commons License

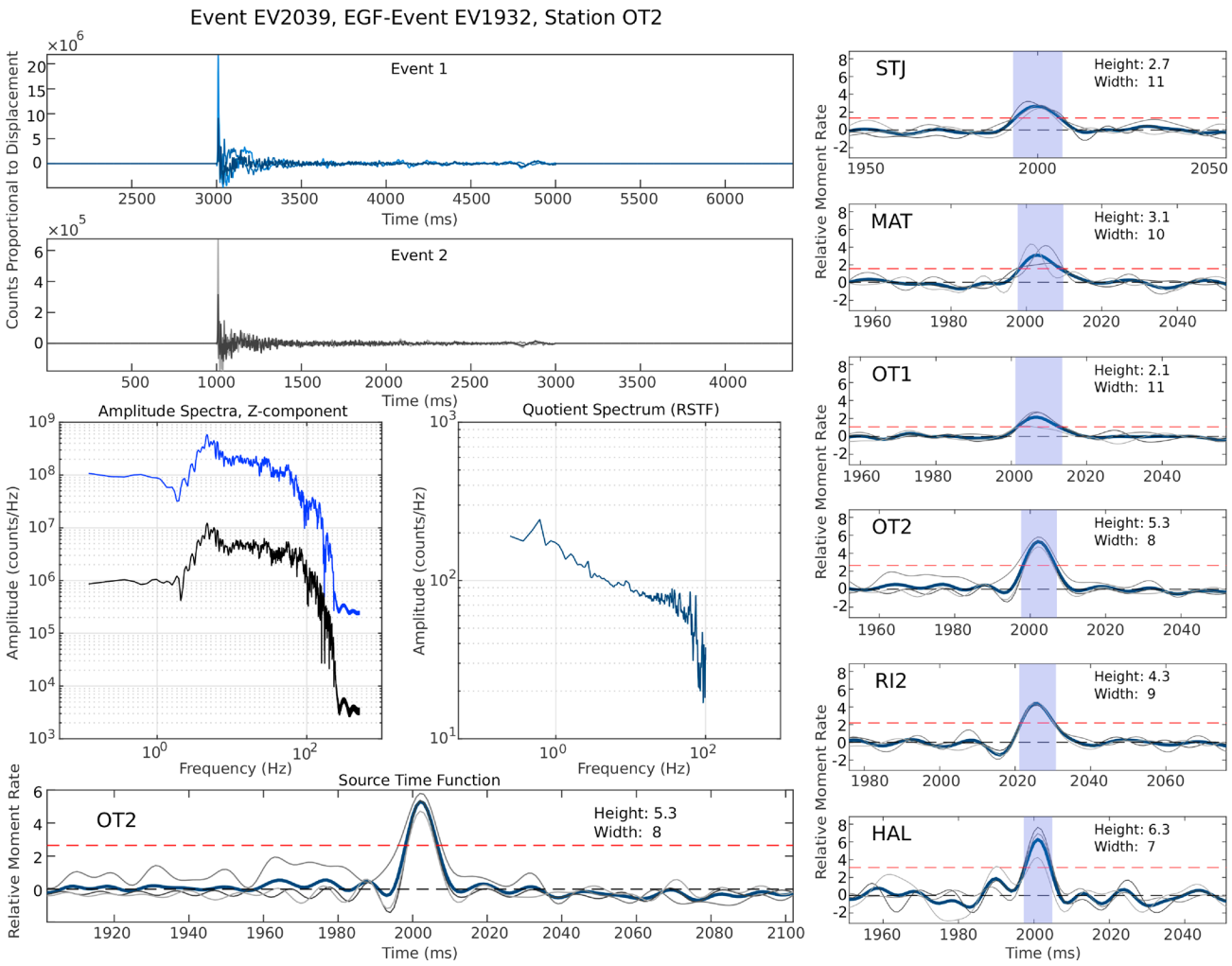

Figure 3. (left column) Reconstruction of the relative source time function (RSTF) for the event Ev_{2039} and its EGF event Ev_{1932} for station OT2. The two top panels show the three-component records of the corresponding *S* phases (note the amplitude difference). Below, the *z* component amplitude spectra and their quotient are shown in respective colors. At the bottom, RSTFs in time domain for each component (gray) and their average (blue) is shown in units of relative moment rate. Dashed lines represent the background amplitude level and the value of half the maximum height at which the pulse width is measured (FWHM). (right column) RSTFs at all six Basel stations. Note the consistent variation of width and height due to the directivity effect, indicated by the blue bar.

RSTF components cannot be properly reconstructed it is discarded. Thus, at least two components contribute to the result. Amplitude and width of the resulting RSTF are then computed. A data example illustrating the processing and the systematic variation of amplitude and width of the RSTFs with station azimuth is shown in Figure 3.

A rough estimate using both *Eshelby* [1957] (circular) or *Knopoff* [1958] (rectangular, unilateral) rupture models, and assuming stress drops of 1–10 MPa [e.g., *Goertz-Allmann et al.*, 2011], yields source time function widths (durations) of a few tens of milliseconds, suggesting that the sampling rate of 1 kHz is sufficient to resolve directivity at this scale ($0.90 \leq M_L \leq 2.35$). In spite of the fact that the variation of pulse width is in principle resolvable, we follow the approach of *Jost et al.* [1998] who found that the fit using the RSTF amplitudes (equation (3)) rather than the durations (equation (4)) produces the more reliable results. The measured amplitude values at all stations are compared, and unreasonable small and large data points are removed by neglecting values smaller than one fifth of the mean of all measured amplitudes, which is approximately the minimum expected amplitude based on a rupture velocity of 0.8 times the *S* wave velocity. The upper limit is empirically set to 5 times the mean amplitude. We require a minimum number of five RSTF amplitude values for the fit. We fit both the unilateral and the bilateral implementations of equation (3), and we choose the result with the lower RMS. Since we consider a multivariable problem with only few measurement values, we assume that the fault plane is subvertical and that the rupture within this plane propagates horizontally

21699356, 2016, 11, Downloaded from https://agupubs.onlinelibrary.wiley.com/doi/10.1002/2016JB013078 by Cochrane Germany, Wiley Online Library on [23/01/2024]. See the Terms and Conditions (https://onlinelibrary.wiley.com/terms-and-conditions) on Wiley Online Library for rules of use; OA articles are governed by the applicable Creative Commons License

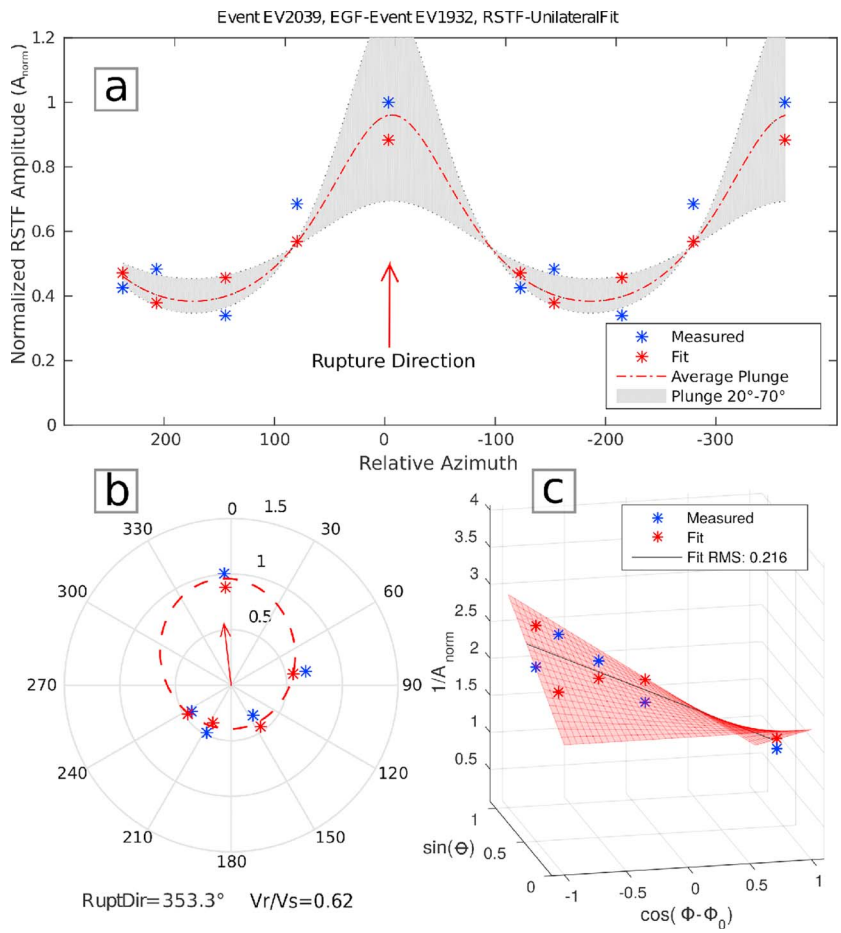

Figure 4. Graphical representations of the amplitude-directivity fit. For the fit formula (3) is rearranged in the following way: $[1/A_i = a_i - b_i(\cos^i(\phi - \phi_0) * \sin^i(\theta))]$. Further is $b^i/a^i = (v_r/v_s)^{1/2}$. Measured values are blue. Red asterisks show fitted amplitude values including the respective station plunge correction. For a simplified graphical representation a hypothetical average plunge is computed for all stations, allowing a representation of the fitted data as the (a) red curve or in (b) planar view. The strong influence of the plunge is indicated by a gray corridor of plunge values of 20°–70°. Since all stations have individual plunges, the red asterisks do not lie on the curve. (c) The fitting result can alternatively be visualized by a surface through the red data points.

(cf. Figure 2); hence, θ_0 is set to zero. This is a reasonable assumption, since the predominant mechanisms in the reservoir are strike-slip and oblique events close to strike slip [*Kraft and Deichmann*, 2014], which implies that the fracture growth is due to shear stress and that the rupture propagates in the direction of slip (fracture mode II). As the directivity effect is a 3-D phenomenon, we must account for the take off angle of the ray at the source, the plunge θ, between individual stations and the rupture. For this reason we use the take off angle from the localization study, performed using the grid search-based, probabilistic earthquake localization code *NonLinLoc* [*Lomax et al.*, 2000]. Subsequently, the fitting procedure from *Li et al.* [1995] must be extended in order to comprise the individual station plunges. For this multivariable minimization problem we use the non-linear problem solver fmincon provided in MATLAB®. It minimizes the misfit between measured data and the given model of amplitude variation and yields the rupture directivity direction. Graphically, the problem can be represented as a surface through the amplitude data (cf. Figure 4). In the teleseismic context the impact of the plunge is often ignored [e.g., *Kanamori and Anderson*, 1975] because of the large epicentral distances between stations and events and the comparatively small source depth. The fit then yields the rupture velocity ratio v_r/v_s and the direction of the rupture ϕ_0. It is difficult to quantify the uncertainty of even single EGFs and subsequently the quality of the direction estimates. In a detailed study *Abercrombie* [2015] concluded that a minimum of five records or stations per event are sufficient for a reasonable source parameter reconstruction with less than 10% uncertainty. In our case this issue was addressed by testing our algorithm using

21699356, 2016, 11, Downloaded from https://agupubs.onlinelibrary.wiley.com/doi/10.1002/2016JB013078 by Cochrane Germany, Wiley Online Library on [23/01/2024]. See the Terms and Conditions (https://onlinelibrary.wiley.com/terms-and-conditions) on Wiley Online Library for rules of use; OA articles are governed by the applicable Creative Commons License

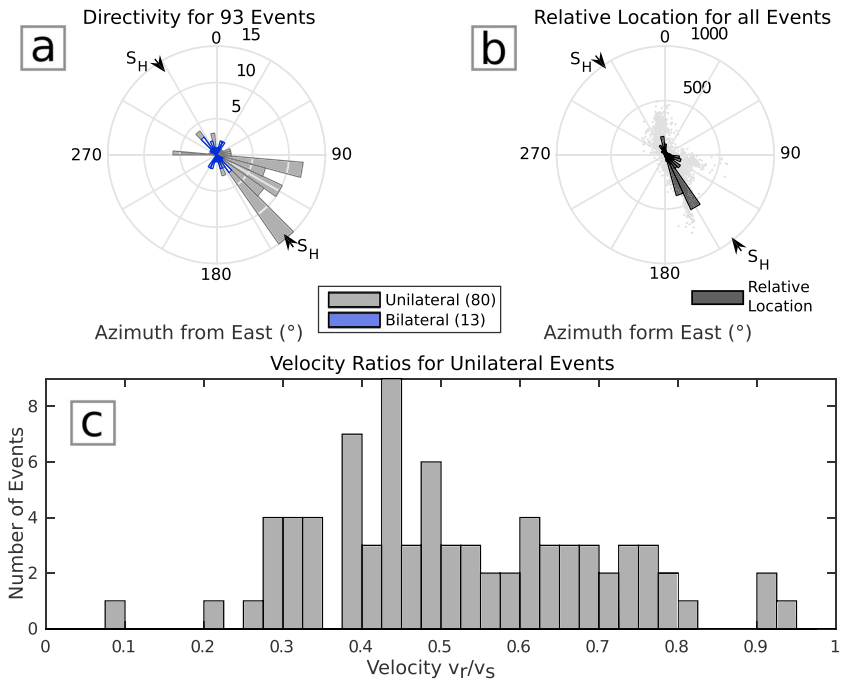

Figure 5. (a) Distribution of rupture directivity estimates. Note that the unilateral solutions predominate. There exists a clear trend in southeast direction. S_H is the direction of the maximum horizontal stress. (b) Diagram of number of event locations relative to the borehole. (c) Velocity estimates relative to *S* wave velocity. Note the broad variation of velocities. Note also that the velocity estimates only represent the horizontal rupture velocity.

synthetic Haskell-type ruptures which were modeled using a FD algorithm [*Saenger et al.*, 2000]. For the tests we first used a circle of 12 azimuthally evenly distributed stations which produced results with directivity estimates with less than 2% error. In a second step we modeled the station-event geometry of the Basel EGS and found that rupture directivity and velocities were reconstructed reliably with estimates that showed less than 5% deviation from the modeled rupture directions.

5. Results

For 93 out of 195 events we find robust signatures of azimuth-dependent amplitude variations which allow to compute rupture directivity and rupture speed. A statistical overview of the distribution of events with directional behavior is shown in Figure 5. Unilateral behavior seems to prevail (80 events), and only a small group of events (13 events) is best fit as bilateral. Therefore, we decided to focus here on the events with unilateral directivity estimates. We observe that the rupture directivity estimates show a clear and dominant trend in southeast direction (Figure 5a). Only few events rupture in the opposite direction (toward northwest), and contributions of other directions are also relatively small. For comparison Figure 5b shows the distribution of hypocenters of all event locations at Basel. Both distributions in Figures 5a and 5b are partly consistent. The fit routine also produces rupture velocity estimates (for further details see *Li et al.* [1995]). We find values for rupture velocities normalized to the *S* wave speed, v_r/v_s, that range from 0.1 to 0.9. Note, however, that the velocities are true velocities only if the rupture direction is horizontal. The spatial overview of the estimated directivity for the 80 unilateral events is given in Figure 6, where rupture directivity is indicated by an arrow at the hypocenter location of each event. In the vicinity of the open hole section of the borehole (red line), the rupture directivity follows no clear trend, and rupture directions different from southeast or northwest are observed. At a greater distance directivity shows a preferred orientation and is directed mainly toward the southeast direction. In the spatiotemporal event domain (Figure 7), the seismicity can be separated into two phases. No clear trend in the rupture directivity is observed during the first 3 days. Here rupture directivity varies broadly and shows an only weak tendency toward northwest or southeast. Events in this phase are located close to the borehole. The second phase, starting at day 3, covers events that show directivity almost exclusively toward southeast. This phase includes the majority of the events used in this study. It is notable

21699356, 2016, 11, Downloaded from https://agupubs.onlinelibrary.wiley.com/doi/10.1002/2016JB013078 by Cochrane Germany, Wiley Online Library on [23/01/2024]. See the Terms and Conditions (https://onlinelibrary.wiley.com/terms-and-conditions) on Wiley Online Library for rules of use; OA articles are governed by the applicable Creative Commons License

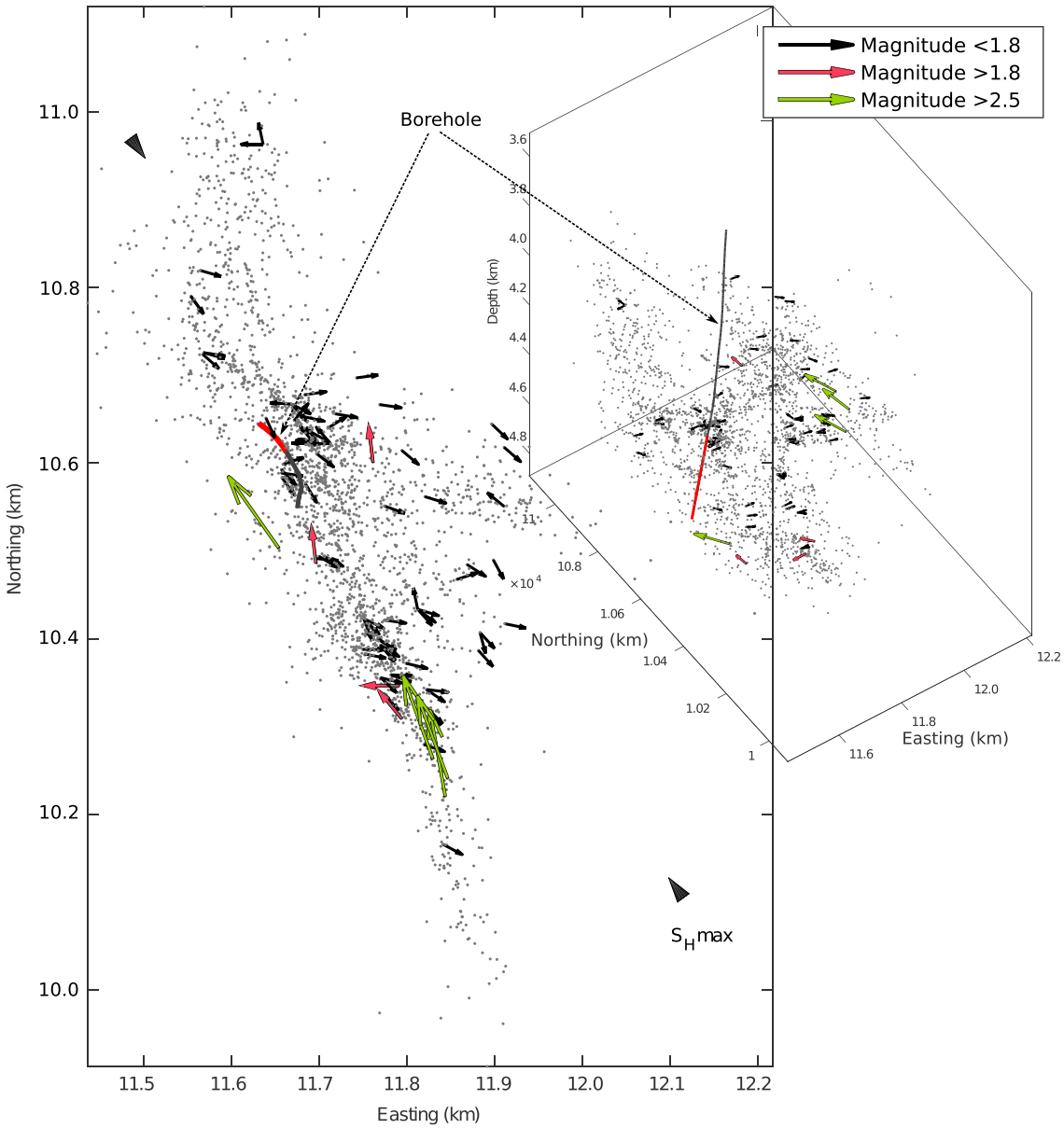

Figure 6. Rupture directivity and microseismic cloud in map view and in side view. Arrows represent rupture directivity estimates. Location of nucleation (hypocenter) is at the tail of each arrow. Events with $M_L < 1.8$ are colored black. Events with $M_L \geq 1.8$ are color coded red. These are the largest events within this study, showing stable solutions under EGF analysis. Using Back Projection Imaging *Folesky et al.* [2015] reconstructed the paths of the largest events in the reservoir ($3.1 \leq M_L \leq 3.4$). The respective rupture directions are shown in green. Note that the rupture directions of the large events do not follow the main direction trend but rather point inward the microseismic cloud and toward the borehole.

that the largest events from this study ($M \geq 1.8$) occurred during a short period slightly before and after the shut-in of the Basel stimulation. The rupture directions of these events do not follow the main trend but point in the opposite direction, i.e., back inside the reservoir and toward the injection source. The spatial distance of the largest events from the borehole is relatively large (about 230 m–450 m). The map and side view in Figure 6 reveal that all four large events (red) are located close to the boundaries of the stimulated volume, which was even smaller than displayed by the time of their occurrence.

The second half of events that were analyzed in this study do not show significant or consistent enough attributes for a directivity estimate. This could be due to one of the following reasons:

1. The rupture process is not strongly directional. This is the case for circular faults rupturing in all directions within the fault plane almost simultaneously, or alternatively an instantaneous rupture on a fault plane.

21699356, 2016, 11, Downloaded from https://agupubs.onlinelibrary.wiley.com/doi/10.1002/2016JB013078 by Cochrane Germany, Wiley Online Library on [23/01/2024]. See the Terms and Conditions (https://onlinelibrary.wiley.com/terms-and-conditions) on Wiley Online Library for rules of use; OA articles are governed by the applicable Creative Commons License

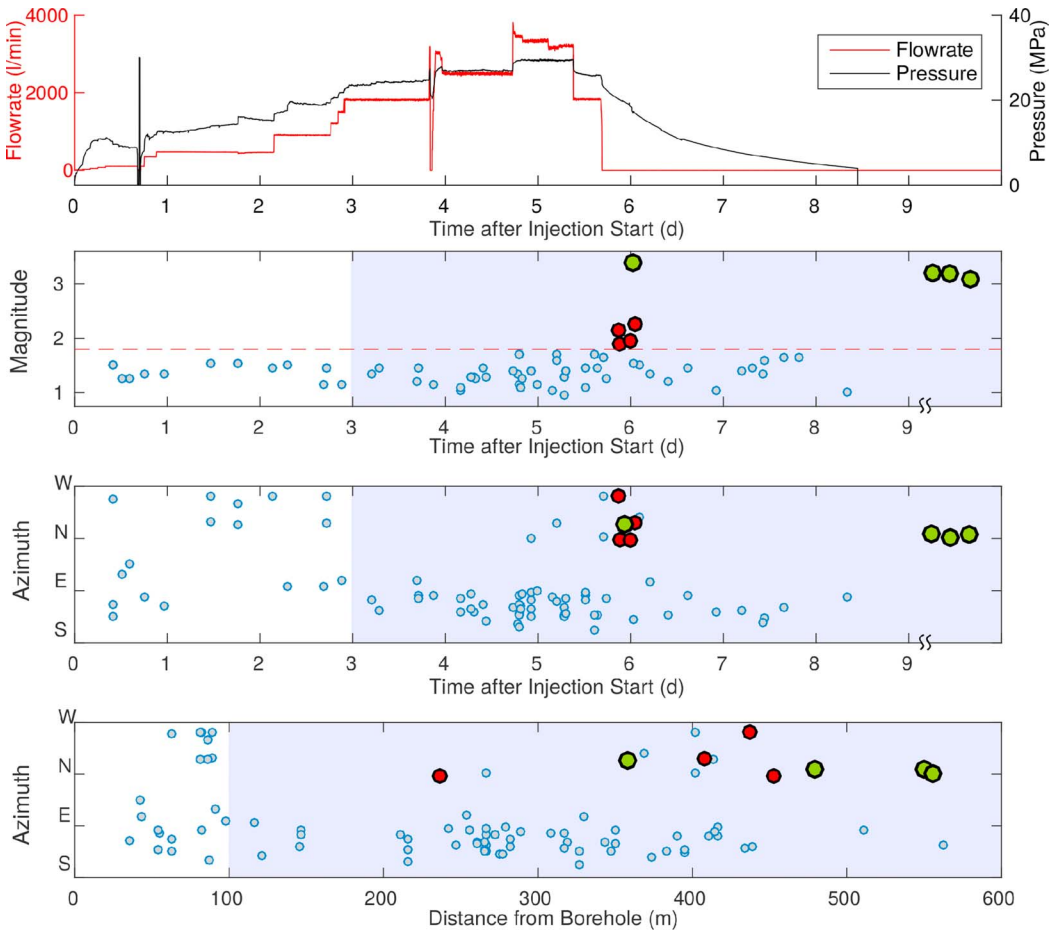

Figure 7. Magnitude and rupture directivity for 80 events with stable directivity estimates. The observed directivity can be divided into two phases. First (white) is the injection phase until day 3, where no significant trend of directivity is found. Second (blue) is the phase after day 3, where a clear trend of directivity toward the southeast is observed. Spatial partitioning corresponds to the temporal phases one and two. In the vicinity of the open hole no clear trend of directivity is found. Beginning at 100 m distance a clear southeast trend occurs. The four largest events ($M > 1.8$) from this study are color coded in red. Green are the largest events at Basel ($M > 3.2$, directivity from a Back Projection study by *Folesky et al.* [2015]). All eight large events do not obey the prevalent directivity, and their distance from the borehole is relatively large (230–560 m).

2. The directivity is not resolvable with our approach due to noise or inadequate receiver-rupture geometry. In our case a vertically propagating rupture on a vertical fault would constitute such a scenario.
3. If several subsequent events interfere the rupture becomes complex. Each subevent may be directional, but their superposition cancels out or disturbs the observation of the directivity.

Most of the nondirectional events fall into the above categories 1 and 2, but we also found events which clearly exhibit rupture complexities. Their RSTFs are shown for four azimuthally well distributed seismic receivers in Figure 8. All RSTFs exhibit complexities, which clearly shows they are not single pulse-like functions. Instead, they are characterized by two or even three distinct pulses, which are consistently observed at all stations. Time separation between individual pulses is of the order of 15 ms and is constant for each subevent from station to station, which is an unambiguous indication for colocation of the subevents. The corresponding seismograms for event EV0983 at stations OT2 and RI2 are shown in Figure 9. At receiver OT2, which is located at 2.7 km depth (cf. Figure 1), closest to the microseismic event cloud and therefore records the highest frequencies, the individual subevents are well discernible in the seismograms. The remaining receivers are installed at shallower depths at 320–1200 m below the surface in sedimentary layers, which is why individual subevents are barely identifiable in the waveforms at RI2. The complexity of the rupture process is only resolved by the RSTF at those stations. In all four cases the largest subevent shows a systematic variation of amplitude and duration. For event EV2537, the smaller subevents (blue in Figure 8) exhibit a

21699356, 2016, 11, Downloaded from https://agupubs.onlinelibrary.wiley.com/doi/10.1002/2016JB013078 by Cochrane Germany, Wiley Online Library on [23/01/2024]. See the Terms and Conditions (https://onlinelibrary.wiley.com/terms-and-conditions) on Wiley Online Library for rules of use; OA articles are governed by the applicable Creative Commons License

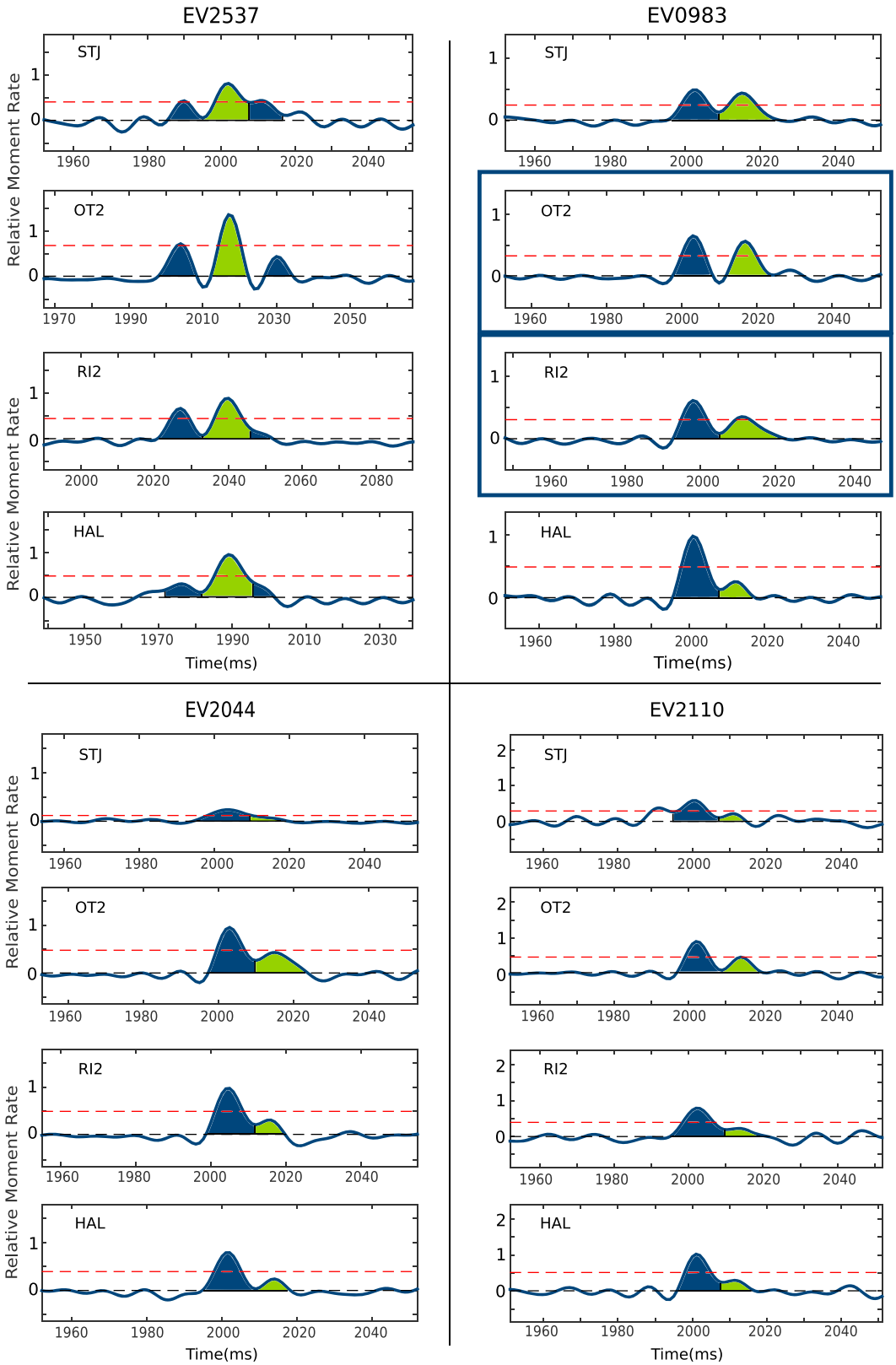

Figure 8. RSTFs of four events at the Basel EGS site at four different receivers, respectively. The RSTFs show complex forms, consistently. Distinct pulses are color coded for enhanced visibility. Each pulse can be interpreted as a rupture or one phase of rupture. Multiple pulses would then constitute either multiple ruptures or one complex, multiphase rupture. The variation of amplitudes indicates a directivity in the rupture process but can be divergent between pulses.

21699356, 2016, 11, Downloaded from https://agupubs.onlinelibrary.wiley.com/doi/10.1002/2016JB013078 by Cochrane Germany, Wiley Online Library on [23/01/2024]. See the Terms and Conditions (https://onlinelibrary.wiley.com/terms-and-conditions) on Wiley Online Library for rules of use; OA articles are governed by the applicable Creative Commons License

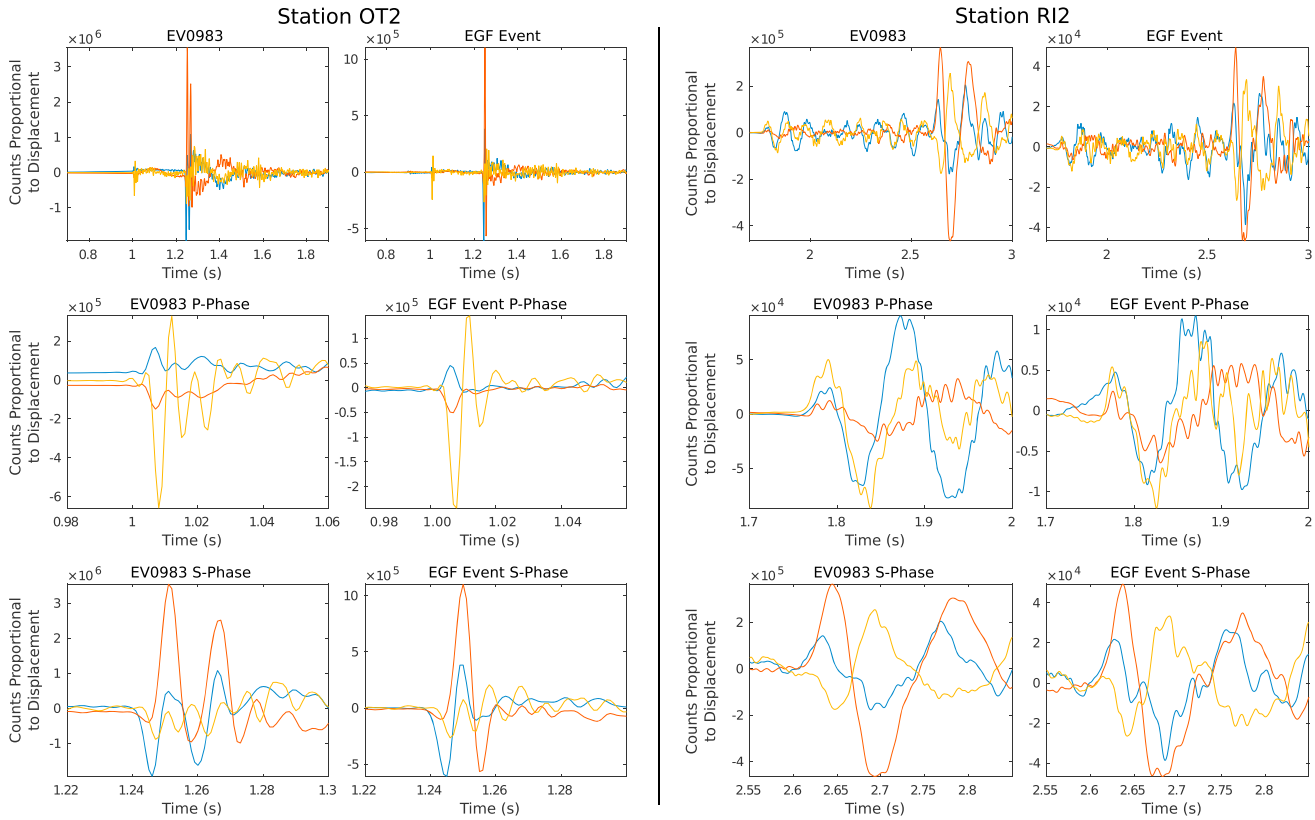

Figure 9. Seismograms for the event EV0983 and its EGF as observed at the two stations (left columns) OT2 and (right columns) RI2. The corresponding RSTFs are framed in blue in Figure 8. (top row) The three-component displacement waveforms. (middle row) A zoom in on the *P* phase. (bottom row) The *S* phase is shown. Note that the EGF waveform at OT2 consist of one pulse or sinusoid per phase. In contrast, the larger event shows a superposition of two wave trains of similar type. At receiver RI2, which resembles lower frequency content, this effect is much harder to identify; however, the RSTF reconstruction in Figure 8 reliably identifies the same two distinct pulses as for station OT2.

similar station-dependent variation of amplitude as the main pulse (green in Figure 8). In the other examples subevents are not coherent with the largest pulse (see especially EV0983 in Figure 8). Given the small time delay between the subevents of about 15 ms, and estimated rupture radii for the examined $M_L \sim 1$ events in the order of tens of meters (assuming stress drop values in the range of 1–10 MPa [*Goertz-Allmann et al.*, 2011]), the subevents probably rupture different parts of the same fault patch and are separated no more than a few tens of meters. Variations of rupture directivity, as evidenced by the RSTF, then indicate small-scale heterogeneity, i.e., asperities, along the ruptured segment. Complexities in the rupture process are principally known to exist in large and medium-sized earthquakes [*Velasco et al.*, 1994; *Li et al.*, 1995], and *Dreger et al.* [2007] and *Taira et al.* [2015] also found evidence for complex rupture processes, i.e., heterogeneous slip distribution and rupture directivity in small natural earthquakes. However, this has rarely been observed for fluid-induced microseismic events.

6. Discussion

The observation of unilateral and bilateral directivity and the resolution of rupture complexities at Basel demonstrate that not only directivity persists in microseismic events but also that heterogeneities can be relevant for small-scale ruptures. These observations contradict the customary approach in microseismic studies which assumes a nondirectional rupture process, where circular rupture models [*Brune*, 1970; *Boatwright*, 1980] are invoked to infer source properties including stress drop or source radius. These models often ignore the influence of rupture directivity by averaging over the entire focal sphere [*Kaneko and Shearer*, 2014].

In the following we discuss the observed directivity and its spatiotemporal characteristics at the Basel EGS in more detail. Figures 6 and 7 show that rupture directivity of events in the close vicinity of the open hole

21699356, 2016, 11, Downloaded from https://agupubs.onlinelibrary.wiley.com/doi/10.1002/2016JB013078 by Cochrane Germany, Wiley Online Library on [23/01/2024]. See the Terms and Conditions (https://onlinelibrary.wiley.com/terms-and-conditions) on Wiley Online Library for rules of use; OA articles are governed by the applicable Creative Commons License

section follows no preferential direction. Here the event-density is generally highest, and we find the same trend for events occurring in the early phase of the experiment, before day 3. We consider the decrease of effective normal stress by the increase of the pore pressure due to injection as the controlling mechanism for the rupture process at the early stage. Close to the borehole the stress perturbation is largest, possibly causing preexisting cracks of arbitrary orientation to fail. Starting with day 3 and a distance of about 100 m, the rupture directivity exhibits a different but clear trend: The events rupture preferably toward the southeast. Only few events rupture in the exact opposite direction. Almost no event exhibits directivity toward northeast or southwest. Figure 5 illustrates that this behavior corresponds to the shape of the microseismic cloud, which itself shows the most hypocenter locations and its largest extend in south-south-east direction, relative to the borehole. It seems that the increased number of event occurrences toward south-south-east and the distribution of rupture directivity could be associated.

The direction of maximum horizontal stress, derived by borehole breakouts [*Häring et al.*, 2008], is in direction 144°, and thus, only a small part of rupture directions is well oriented for optimal shear failure conditions (approximately 22°–30° relative to S_{Hmax}). It seems that the orientation and extension of the microseismic cloud is strongly influenced by the preexisting faults and structures at the site, which are reported to be a network of small substructures rather than one main fault [*Kraft and Deichmann*, 2014]. We observe not only an increasingly clearer trend of orientation but also of directivity of the ruptures with distance to the borehole, suggesting that it is probable that either stress field or structure overtake the control over the rupture process at larger distances from the borehole, as the influence of the increased pore pressure due to the water injection decreases [*Catalli et al.*, 2013].

A different and important observation relates to the largest ($M \geq 1.8$) events within this data set (red colored in Figures 6 and 7). These events do not follow the rupture direction trend of south-south-east but point in the opposite direction, back inside the microseismic cloud. *Folesky et al.* [2015] analyzed the rupture behavior of the four largest ($3.2 \leq M_L \leq 3.4$) induced events at the Basel EGS site, using the method of microseismic rupture propagation imaging. Their results are inserted in both figures in green. Unfortunately, it is impossible to apply the EGF method to these events, because they are isolated and no corresponding EGF events could be found. The observations of both studies coincide nicely. The large events at the Basel reservoir appear to rupture from their nucleation point, close to the rim of the microseismic cloud, back inside into the stimulated volume and toward the injection source. The occurrence time corridor of most of the relatively large events is shortly before and after the stop of injection. The occurrence of relatively large events close to the edges of the stimulated volume has been reported previously for other enhanced geothermal systems [*Majer et al.*, 2007]. To explain such a behavior, e.g., *Goertz-Allmann and Wiemer* [2012] proposed a geomechanical model based on an inverse relationship between *b* value and differential stress. A corresponding observation is made in a local seismicity study on aftershock distribution by *Elst and Shaw* [2015]. They report that larger aftershocks tend to occur farther away from the centroid of previous activity than smaller aftershocks which is interpreted as a feature of stress relaxation on the main rupture patch. The direction of rupture, however, is not included in these studies.

An explanation of the observed inward pointing rupture directions of the largest events at Basel is provided by *Shapiro et al.* [2011]. They found that the maximum expected magnitude is related to the geometry of the rock volume and that a fault is more probable to rupture if its surface is located mostly inside the stimulated volume. This concept anticipates that ruptures are orientated mainly in direction toward the injection source—exactly what we observe for the largest induced events at Basel.

7. Conclusions

Based on the well-balanced azimuthal coverage of the seismic monitoring system at the Basel-enhanced geothermal system and the high quality of the recorded seismograms, we have performed a comprehensive study on rupture directivity of microseismic events in the magnitude range $0.90 \leq M_L \leq 2.35$. Using an empirical Green's function method, we observe clear signatures of directivity by systematic amplitude variations of the relative source time functions for about half of the event pairs suitable for this study. This demonstrates that rupture directivity persists down to small, $M_L \sim 1$ fluid-induced events. For few events we identify complex rupture behavior indicating the existence of asperities and heterogeneities at a scale of a few tens of meters, similar to the observations from natural seismicity in California by *Dreger et al.* [2007] and *Taira et al.* [2015]. This implies that the exact estimation of source properties is more complex than generally

21699356, 2016, 11, Downloaded from https://agupubs.onlinelibrary.wiley.com/doi/10.1002/2016JB013078 by Cochrane Germany, Wiley Online Library on [23/01/2024]. See the Terms and Conditions (https://onlinelibrary.wiley.com/terms-and-conditions) on Wiley Online Library for rules of use; OA articles are governed by the applicable Creative Commons License

assumed since rupture complexity and directivity influence the radiation pattern and spectra significantly [*Kaneko and Shearer*, 2015]. Our results are also consistent with the observations of rupture complexities for mining-induced microearthquakes [*Yamada et al.*, 2005; *Kwiatek et al.*, 2011], supporting the concept of self-similar behavior of the rupture process.

The computed rupture directions show a dependence on distance from the injection source and size of the events. The relative diversity of rupture directions close to the injection source and the increasing alignment of rupture directions with larger distances coincide with the decreasing effect of the pore pressure with larger distances, which also seems to control the observed stress drop [*Goertz-Allmann et al.*, 2011] and role of Coulomb stress changes [*Catalli et al.*, 2013] at Basel. The distinct behavior of the largest events, which rupture preferentially backward to the injection source agrees with independent observations from direct rupture imaging of $M_L \geq 3.2$ events at Basel [*Folesky et al.*, 2015]. These events also occur close to the boundary of the stimulated volume. The findings of this study corroborate the model of *Shapiro et al.* [2011] on the maximal expectable magnitude which is based on the assumption that the potential rupture surface needs to be located mainly inside the stimulated reservoir.

Acknowledgments
We thank the sponsors of the PHASE consortium for supporting the research presented in this paper. We are especially grateful to GeoExplorers Ltd. for providing the seismic waveform data. Data, including seismic waveforms for the EGF pairs, used in this study can be obtained upon request from the corresponding author at jonas.folesky@geophysik.fu-berlin.de. We greatly appreciate the detailed and constructive comments from Martin Mai, an anonymous reviewer, and the Editors who helped us to significantly increase the quality of the paper.

References

Abercrombie, R. E. (2015), Investigating uncertainties in empirical Green's function analysis of earthquake source parameters, *J. Geophys. Res. Solid Earth*, *120*(6), 4263–4277, doi:10.1002/2015JB011984.

Ben-Menahem, A. (1961), Radiation of seismic surface- waves from finite moving sources, *Bull. Seismol. Soc. Am.*, *51*, 401–435, doi:10.1029/91JB01936.

Boatwright, J. (1980), A spectral theory for circular seismic sources: Simple estimates of source dimension, dynamic stress drop, and radiated seismic energy, *Bull. Seismol. Soc. Am.*, *70*(1), 1–27.

Boatwright, J. (2007), The persistence of directivity in small earthquakes, *Bull. Seismol. Soc. Am.*, *97*(6), 1850–1861, doi:10.1785/0120050228.

Boatwright, J., and D. M. Boore (1982), Analysis of the ground accelerations radiated by the 1980 Livermore Valley earthquakes for directivity and dynamic source characteristics, *Bull. Seismol. Soc. Am.*, *72*(6A), 1843–1865.

Brune, J. N. (1970), Tectonic stress and the spectra of seismic shear waves from earthquakes, *J. Geophys. Res.*, *75*(26), 4997–5009, doi:10.1029/JB075i026p04997.

Catalli, F., M. Meier, and S. Wiemer (2013), The role of Coulomb stress changes for injection-induced seismicity: The Basel enhanced geothermal system, *Geophys. Res. Lett.*, *40*(72–77), doi:10.1029/2012GL054.147.

Deichmann, N., and D. Giardini (2009), Earthquakes induced by the stimulation of an enhanced geothermal system below Basel (Switzerland), *Seismol. Res. Lett.*, *80*(5), 784–798, doi:10.1785/gssrl.80.5.784.

Dinske, C., and S. Shapiro (2010), Interpretation of microseismicity induced by timpe-dependent injection pressure, *SEG Expanded Abstr.*, *29*, 2125–2129, doi:10.1190/1.3513.264.

Dreger, D., R. M. Nadeau, and A. Chung (2007), Repeating earthquake finite source models: Strong asperities revealed on the San Andreas Fault, *Geophys. Res. Lett.*, *34*(23), L23302, doi:10.1029/2007GL031353.

Dyer, B., U. Schanz, T. Spillmann, F. Ladner, and M. Häring (2010), Application of microseismic multiplet analysis to the Basel geothermal reservoir stimulation events, *Geophys. Prospect.*, *58*(5), 791–807, doi:10.1111/j.1365-2478.2010.00902.x.

Elst, N. J., and B. E. Shaw (2015), Larger aftershocks happen farther away: Nonseparability of magnitude and spatial distributions of aftershocks, *Geophys. Res. Lett.*, *42*(14), 5771–5778, doi:10.1002/2015GL064734.

Eshelby, J. D. (1957), The determination of the elastic field of an ellipsoidal inclusion, and related problems, *Proc. R. Soc. London, Ser. A*, *241*, 376–396, doi:10.1098/rspa.1957.0133.

Folesky, J., J. Kummerow, and S. A. Shapiro (2015), Microseismic rupture propagation imaging, *Geophysics*, *80*(6), WC107–WC115, doi:10.1190/geo2014-0572.1.

Frankel, A., and H. Kanamori (1983), Determination of rupture duration and stress drop for earthquakes in Southern California, *Bull. Seismol. Soc. Am.*, *73*(6A), 1527–1551.

Frankel, A., J. Fletcher, F. Vernon, L. Haar, J. Berger, T. Hanks, and J. Brune (1986), Rupture characteristics and tomographic source imaging of ML 3 earthquakes near Anza, Southern California, *J. Geophys. Res.*, *91*(B12), 12,633–12,650, doi:10.1029/JB091iB12p12633.

Goertz-Allmann, B. P., and S. Wiemer (2012), Geomechanical modeling of induced seismicity source parameters and implications for seismic hazard assessment, *Geophysics*, *78*(1), KS25–KS39, doi:10.1190/geo2012-0102.1.

Goertz-Allmann, B. P., A. Goertz, and S. Wiemer (2011), Stress drop variations of induced earthquakes at the Basel geothermal site, *Geophys. Res. Lett.*, *38*(9), doi:10.1029/2011GL047498.

Häring, M. O., U. Schanz, F. Ladner, and B. C. Dyer (2008), Characterisation of the Basel 1 enhanced geothermal system, *Geothermics*, *37*(5), 469–495, doi:10.1016/j.geothermics.2008.06.002.

Harrington, R. M., and E. E. Brodsky (2009), Source duration scales with magnitude differently for earthquakes on the San Andreas Fault and on secondary faults in Parkfield, California, *Bull. Seismol. Soc. Am.*, *99*(4), 2323–2334, doi:10.1785/0120080216.

Haskell, N. (1964), Total energy and energy spectral density of elastic wave radiation from propagating faults, *Bull. Seismol. Soc. Am.*, *54*(6A), 1811–1841.

Jost, M. L., T. Büßelberg, O. Jost, and H.-P. Harjes (1998), Source parameters of injection-induced microearthquakes at 9 km depth at the KTB Deep Drilling site, Germany, *Bull. Seismol. Soc. Am.*, *88*(3), 815–832.

Kanamori, H., and D. L. Anderson (1975), Theoretical basis of some empirical relations in seismology, *Bull. Seismol. Soc. Am.*, *65*, 1073–1095.

Kane, D. L., P. M. Shearer, B. P. Goertz-Allmann, and F. L. Vernon (2013), Rupture directivity of small earthquakes at Parkfield, *J. Geophys. Res. Solid Earth*, *118*(1), 212–221, doi:10.1029/2012JB009675.

Kaneko, Y., and P. M. Shearer (2014), Seismic source spectra and estimated stress drop derived from cohesive-zone models of circular subshear rupture, *Geophys. J. Int.*, *197*(2), 1002–1015, doi:10.1093/gji/ggu030.

Kaneko, Y., and P. M. Shearer (2015), Variability of seismic source spectra, estimated stress drop, and radiated energy, derived from cohesive-zone models of symmetrical and asymmetrical circular and elliptical ruptures, *J. Geophys. Res. Solid Earth*, *120*(2), 1053–1079, doi:10.1002/2014JB011642.

21699356, 2016, 11, Downloaded from https://agupubs.onlinelibrary.wiley.com/doi/10.1002/2016JB013078 by Cochrane Germany, Wiley Online Library on [23/01/2024]. See the Terms and Conditions (https://onlinelibrary.wiley.com/terms-and-conditions) on Wiley Online Library for rules of use; OA articles are governed by the applicable Creative Commons License

Knopoff, L. (1958), Energy release in earthquakes, *Geophys. J. Int.*, *1*(1), 44–52, doi:10.1111/j.1365-246X.1958.tb00033.x.
Kraft, T., and N. Deichmann (2014), High-precision relocation and focal mechanism of the injection-induced seismicity at the Basel EGS, *Geothermics*, *52*, 59–73, doi:10.1016/j.geothermics.2014.05.014.
Kummerow, J., S. Shapiro, H. Asanuma, and M. Häring (2011), *Application of an Arrival Time and Cross Correlation Value-Based Location Algorithm to the Basel 1 Microseismic Data*, Expanded Abstracts, EAGE 73nd annual meeting and technical exhibition, Vienna.
Kummerow, J., S. Shapiro, H. Asanuma, and M. Häring (2014), *Observation and Signatures of Injection-Induced Repeating Earthquake Sequences*, Expanded Abstracts, EAGE 76th annual meeting and technical exhibition, Vienna.
Kwiatek, G., et al. (2011), Source parameters of picoseismicity recorded at Mponeng deep gold mine, South Africa: Implications for scaling relations, *Bull. Seismol. Soc. Am.*, *101*(6), 2592–2608, doi:10.1785/0120110094.
Li, Y., C. Doll, and M. N. Toksöz (1995), Source characterization and fault plane determination for MbLg = 1.2 to 4.4 earthquakes in the Charlevoix Seismic Zone, Quebec, Canada, *Bull. Seismol. Soc. Am.*, *85*(6), 1604–1621.
Lomax, A., J. Virieux, P. Volant, and C. Berge-Thierry (2000), Probabilistic earthquake location in 3D and layered models, in *Advances in seismic event location*, pp. 101–134, Springer, Kluwer, Amsterdam., doi:10.1007/978-94-015-9536-0_5
Madariaga, R. (1976), Dynamics of an expanding circular fault, *Bull. Seismol. Soc. Am.*, *66*(3), 639–666.
Majer, E. L., R. Baria, M. Stark, S. Oates, J. Bommer, B. Smith, and H. Asanuma (2007), Induced seismicity associated with enhanced geothermal systems, *Geothermics*, *36*(3), 185–222, doi:10.1016/j.geothermics.2007.03.003.
McGuire, J. J., L. Zhao, and T. H. Jordan (2002), Predominance of unilateral rupture for a global catalog of large earthquakes, *Bull. Seismol. Soc. Am.*, *92*(8), 3309–3317, doi:10.1785/0120010293.
Mori, J. (1993), Fault plane determinations for three small earthquakes along the San Jacinto fault, California: Search for cross faults, *J. Geophys. Res.*, *98*(B10), 17,711–17,722, doi:10.1029/93JB01229.
Mueller, C. S. (1985), Source pulse enhancement by deconvolution of an empirical Green's function, *Geophys. Res. Lett.*, *12*, 33–36, doi:10.1029/GL012i001p00033.
Reshetnikov, A., J. Kummerow, H. Asanuma, M. Häring, and S. A. Shapiro (2015), Microseismic reflection imaging and its application to the Basel geothermal reservoir, *Geophysics*, *80*(6), WC39–WC49, doi:10.1190/geo2014-0593.1.
Saenger, E. H., N. Gold, and S. A. Shapiro (2000), Modeling the propagation of elastic waves using a modified finite-difference grid, *Wave Motion*, *31*(1), 77–92, doi:10.1016/S0165-2125(99)00023-2.
Savage, J. C. (1965), The effect of rupture velocity upon seismic first motions, *Bull. Seism. Soc. Am.*, *55*, 263–275.
Shapiro, S. A., O. S. Krüger, C. Dinske, and C. Langenbruch (2011), Magnitudes of induced earthquakes and geometric scales of fluid-stimulated rock volumes, *Geophysics*, *76*(6), WC55–WC63, doi:10.1190/geo2010-0349.1.
Taira, T., D. S. Dreger, and R. M. Nadeau (2015), Rupture process for micro-earthquakes inferred from borehole seismic recordings, *Int. J. Earth Sci.*, *104*(6), 1499–1510, doi:10.1007/s00531-015-1217-8.
Vallée, M. (2004), Stabilizing the empirical Green function analysis: Development of the projected Landweber method, *Bull. Seismol. Soc. Am.*, *94*(2), 394–409, doi:10.1785/0120030017.
Velasco, A. A., C. J. Ammon, and T. Lay (1994), Recent large earthquakes near Cape Mendocino and in the Gorda plate: Broadband source time functions, fault orientations, and rupture complexities, *J. Geophys. Res.*, *99*, 711–728, doi:10.1029/93JB02390.
Yamada, T., J. J. Mori, S. Ide, H. Kawakata, Y. Iio, and H. Ogasawara (2005), Radiation efficiency and apparent stress of small earthquakes in a South African gold mine, *J. Geophys. Res.*, *110*, B01305, doi:10.1029/2004JB003221.

Erratum

In the originally published version of this article, there was an error in equation 3 and in the sentence after the equation. The errors have been corrected, and this may be considered the authoritative version of record.

21699356, 2016, 11, Downloaded from https://agupubs.onlinelibrary.wiley.com/doi/10.1002/2016JB013078 by Cochrane Germany, Wiley Online Library on [23/01/2024]. See the Terms and Conditions (https://onlinelibrary.wiley.com/terms-and-conditions) on Wiley Online Library for rules of use; OA articles are governed by the applicable Creative Commons License